Heliyon 10 (2024) e24016

Contents lists available at ScienceDirect

Heliyon

journal homepage: www.cell.com/heliyon

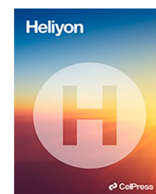

Research article

Focused solar annealing for block copolymer fast self-assembly

Xiao-Hua Hu [a,2,1], Rui Zhang [a,2,1], Xiaohui Zhang [b], Zhiyong Wu [a], Jing Zhou [a], Weihua Li [b,**], Shisheng Xiong [a,c,*]

[a] School of Information Science and Technology, Fudan University, 220 Handan Road, Shanghai, 200433, China
[b] Department of Macromolecular Science, Fudan University, 220 Handan Road, Shanghai, 200433, China
[c] Zhangjiang Laboratory, 100 Haike Road, Shanghai, 201204, China

ARTICLE INFO

Keywords:
Block copolymer
Fast self-assembly
Focused solar annealing
Contact hole shrinking
Contact hole multiplication
Carbon neutrality

ABSTRACT

Block copolymer (BCP) self-assembly has tremendous potential applications in next-generation nanolithography. It offers significant advantages, including high resolution and cost-effectiveness, effectively overcoming the limitations associated with conventional optical lithography. In this work, we demonstrate a focused solar annealing (FSA) technique that is facile, eco-friendly, and energy-efficient for fast self-assembly of polystyrene-*block*-poly(methyl methacrylate) (PS-*b*-PMMA) thin films. The FSA principle involves utilizing a common biconvex lens to converge incident solar radiation into a high-temperature spot, which is directly used to drive the microphase separation of PS-*b*-PMMA thin films. As a result, PS-*b*-PMMA undergoes self-assembly, forming ordered nanostructures in a vertical orientation at seconds timescales on silicon substrates with a neutral layer. In addition, the FSA technique can be employed for grafting neutral polymer brushes onto the silicon substrate. Furthermore, the FSA's compatibility with graphoepitaxy-directed self-assembly (DSA) of BCP is also demonstrated in the patterning of contact holes. The results of contact hole shrinking show that contact hole prepatterns of ~60.4 nm could be uniformly shrunk to ~20.5 nm DSA hole patterns with a hole open yield (HOY) of 100 %. For contact hole multiplication, doublet DSA holes were successfully generated on elliptical templates, revealing an average DSA hole size of ~21.3 nm. Most importantly, due to the direct use of solar energy, the FSA technique provides many significant advantages such as simplicity, environmental friendliness, solvent-free, low cost, and net-zero carbon emissions, and will open up a new direction for BCP lithography that is sustainable, pollution-free, and carbon-neutral.

1. Introduction

Today, we are living in an era of unprecedented high technology and economic prosperity. However, we still face some severe challenges, such as global warming [1]. Since the industrial revolution, excessive consumption of fossil fuels caused a rapid increase in carbon emissions into the atmosphere, which was the main reason for global warming [2]. Global warming can breed various natural

* Corresponding author. School of Information Science and Technology, Fudan University, 220 Handan Road, Shanghai 200433, China.
** Corresponding author.
E-mail addresses: weihuali@fudan.edu.cn (W. Li), sxiong@fudan.edu.cn (S. Xiong).
[1] Co-first Author.
[2] Xiao-Hua Hu and Rui Zhang contributed equally to this work.

https://doi.org/10.1016/j.heliyon.2024.e24016
Received 8 August 2023; Received in revised form 23 December 2023; Accepted 2 January 2024
Available online 5 January 2024
2405-8440/© 2024 Published by Elsevier Ltd. This is an open access article under the CC BY-NC-ND license (http://creativecommons.org/licenses/by-nc-nd/4.0/).

disasters such as droughts, heatwaves, storms, floods, sea-level rise, and ocean acidification, all of which present a grave threat to the continued existence of life on Earth [2,3]. To combat global warming, carbon neutrality was first proposed in the *Paris Agreement*, which garnered adoption from 196 attending parties on December 12, 2015 [4]. Currently, numerous countries, organizations, and companies have formulated plans to achieve carbon neutrality in the coming years. For example, Intel has implemented diverse strategies to fight global warming, including enhancing energy efficiency, substituting fossil fuels with renewable energy sources, advancing technologies for carbon capture, and engaging in modeling efforts to understand and address global climate change [5]. Among these strategies, adopting new energy sources like solar energy, wind energy, hydropower, and hydrogen energy as alternatives to fossil fuels is widely considered to be the most effective and direct approach. Undoubtedly, solar energy stands out as an optimal alternative energy owing to its numerous notable benefits, including cleanliness, renewability, eco-friendliness, cost-effectiveness, non-toxicity, harmlessness, and inexhaustibility [6–8]. Currently, solar energy is being utilized directly or indirectly for various applications of heat and power generation, including photovoltaic cells, solar air conditioning, solar cooking, solar water heating, solar drying, and nanomaterial preparation [6–10].

As we all know, the manufacturing industry stands as the primary consumer of energy and a major emitter of carbon dioxide [11–14]. Very recently, global semiconductor manufacturers have announced plans to expand chip manufacturing capacities to meet the surge in demand for chips [15–17]. These expansion plans could potentially lead to an increase in carbon emissions and run counter to achieving carbon neutrality. They may also result in an elevated use of potentially hazardous chemicals, including solvents, acids, metals, photoactive materials, and gases required for manufacturing [18]. Current advancements in bottom-up lithography, e.g., block copolymer (BCP) self-assembly, have been identified as potential candidates for the next-generation technology in semiconductor chip production, according to the *International Roadmap for Devices and Systems* (IRDS) [19,20]. BCP self-assembly is highly attractive for semiconductor chip production due to its high resolution, remarkable efficiency, notable scalability, cost-effectiveness, and compatibility with industrial semiconductor processes [20–23]. Furthermore, BCP self-assembly provides an excellent opportunity to enhance the sustainability of lithography and achieve carbon neutrality by minimizing energy consumption, streamlining procedure steps, and mitigating the generation of chemical waste products [18,24]. To date, BCP self-assembly has been employed in the fabrication of diverse devices, including fin field-effect transistors, nonvolatile memory, and photonic nanodevices [20,21].

BCP self-assembly relies on the molecular microphase separation to create high-density and highly-ordered pattern arrays, featuring sizes that range from 5 to 100 nm [21]. The driving force behind self-assembly stems from the thermodynamic incompatibility between the constituent blocks within BCPs [20,21]. However, external energy is still required to overcome the kinetics barrier before the self-assembly process. Thermal annealing is the most commonly employed technique in the community of BCP self-assembly [19,25]. Later, various annealing techniques were developed for BCP self-assembly, including rapid thermal processing [26,27], microwave annealing [28,29], laser annealing [30–33], flash light irradiation [34], and argon-plasma radiation [35]. These new technologies greatly enrich the BCP film self-assembly toolbox and demonstrate their respective merits in some aspects. However, they all need to consume secondary energy (such as electrical energy) to overcome the kinetics barrier of BCP self-assembly process. This would inevitably result in a heightened consumption of non-renewable energy sources, e.g., fossil fuels, consequently contributing to rising carbon emissions.

In this work, a novel, simple, green, no electricity-consuming, and zero-carbon emission annealing technique is first presented for BCP fast self-assembly and named focused solar annealing (FSA). The fundamental principle of the FSA involves utilizing a common biconvex lens to converge the sunlight radiation into a small high-temperature light spot. The high-temperature light spot directly drives BCP microphase separation. The temperature of the concentrated light spot can vary from 50 to 600 °C, depending on the distance between lens and sample. When adjusted to the proper temperature, polystyrene-*block*-poly(methyl methacrylate) (PS-*b*-PMMA) can undergo self-assembly in a short time (~30 s) on silicon substrates coated with a neutral layer, generating highly ordered nanostructures with a perpendicular orientation. In addition, the FSA method can also be applied in the neutral layer grafting process, i.e., grafting neutral polymer brushes onto the surface of silicon substrates. Moreover, the compatibility of the FSA technique with the directed self-assembly (DSA) has been verified in the applications of contact hole shrinking and contact hole multiplication. This results in the production of uniform DSA hole patterns with a diameter of ~21 nm, achieving a hole open yield (HOY) of 100 % over a large area. These results fully demonstrate that the FSA method is a feasible and highly efficient annealing technique that can dramatically reduce energy consumption, process time, cost, and carbon emissions for BCP lithography.

2. Experimental section

2.1. Materials

PS-*b*-PMMA (molecular weight: M_n = 31-*b*-33 kg/mol, bulk period: L_0 = 35.6 nm), PS-*b*-PMMA (molecular weight: M_n = 37-*b*-16.8 kg/mol, bulk period: L_0 = 28.3 nm), PS-*b*-PMMA (molecular weight: M_n = 46.1-*b*-21 kg/mol, bulk period: L_0 = 37.5 nm), hydroxyl-terminated poly(styrene-*co*-methylmethacrylate) (PS-*r*-PMMA, molecular weight: M_n = 8 kg/mol, PS content: 72 mol%), and poly (styrene-*co*-methylmethacrylate-*co*-hydroxyethyl methacrylate) (PS-*r*-PMMA, molecular weight: M_n = 40.7 kg/mol, PS content: 58 mol%) were received from Polymer Source Inc. (Montreal, Canada) and used without any further purification. Statistical poly(styrene-*co*-methylmethacrylate) (PS-*r*-PMMA, molecular weight: M_n = 24.5 kg/mol, PS content: 72.1 mol%) was obtained from Professor Shengxiang Ji (Changchun Institute of Applied Chemistry, Chinese Academy of Sciences, China) and used without any further purification. Toluene (C_7H_8, 99.8 %), acetone (C_3H_6O, 99.5 %), and isopropanol (C_3H_8O, 99.7 %) were brought from Sigma-Aldrich (Shanghai, China). Propylene glycol monomethyl ether acetate (PGMEA) ($C_6H_{12}O_3$, electronic grade) was received from Jiangsu Nata Opto-electronic Material Co., Ltd. (Suzhou, China). Hydrogen peroxide (H_2O_2, 30 %) and concentrated sulfuric acid (H_2SO_4, 98

%) were brought from Sinopharm Chemical Reagent Co., Ltd. (Shanghai, China). Phosphorus-doped silicon wafers with a thickness of 0.5 mm were purchased from Zhejiang MTCN Technology Co., Ltd (Quzhou, China). The ultra-purified and distilled deionized water was sourced from the laboratory of the School of Microelectronics at Fudan University (Shanghai, China).

2.2. BCP self-assembly by FSA

The silicon wafers were precision-cut into square pieces with dimensions of 1×1 cm^2 and 2×2 cm^2, respectively. The silicon substrates underwent a cleaning process through ultrasonication in acetone and isopropanol for 5 min each, followed by drying with a nitrogen (N_2) flow. To enhance the density of hydroxyl groups on the silicon surface, the substrates underwent an additional cleaning step using a 3:1 (v/v) mixture of 98 % H_2SO_4 and 30 % H_2O_2 for 30 min. They were then rinsed multiple times with distilled deionized water and dried with a stream of N_2. PS-*r*-PMMA solution with a concentration of 1.0 wt% in toluene was spin-coated onto the cleaned substrates using a spin coater (LEBO Science EZ6 Spin-coater, China) at 2000 rpm for 60 s. The samples were subjected to annealing in a vacuum oven (UniTemp RSS-110-S, Germany) at 200 °C for 30 min. This procedure results in the formation of chemically anchored random copolymers through condensation reactions between the silanol groups at the silicon substrate surface and on the random copolymers. The substrates were then sonicated in a warm toluene bath to eradicate any ungrafted random copolymers, followed by rinsing with fresh toluene and drying with a stream of N_2. Solutions of PS-*b*-PMMA with a concentration of 0.5 wt% in toluene were spin-coated onto the silicon surfaces that were previously anchored with random copolymers, using a spin-coater at 4000 rpm for 60 s. A spectral reflectometer (Filmetrics F20-UV, USA) was used to quantify the thickness of the resulting PS-*b*-PMMA film.

On a normal sunny day, sunlight was focused with an18 cm biconvex lens to form a spot size of 0.5–2.0 cm on a 2×2 cm^2 bare silicon substrate. The sun's direct radiation passed through the biconvex lens vertically. The temperature of focused sunlight spot on silicon substrates was determined by a digital thermometer (UNI-T UT325, China) with a thin-foil thermocouple. By adjusting the size of the focused spot, the desired annealing temperatures were obtained. Subsequently, the silicon coated with BCP thin films instead of the bare silicon substrate was exposed to focused sunlight at the target temperature for 5–60 s and then cooled down to ambient conditions. The sunlight intensity was determined to be about 1000 W/m^2 (i.e., one sun), by a solar power meter (TES 133R, Chinese Taipei). For comparison, PS-*b*-PMMA (M_n = 31-*b*-33 kg/mol) samples were subjected to thermal annealing at 250 °C for 5 min in a vacuum oven to induce PS-*b*-PMMA microphase separation. Meanwhile, PS-*b*-PMMA (M_n = 37-*b*-16.8 kg/mol) samples were thermally annealed at 220 °C for 15 min in a vacuum oven to achieve self-assembly.

2.3. Sequential infiltration synthesis process

The PS-*b*-PMMA self-assembled nanostructures were transformed into metal oxides through a sequential infiltration synthesis (SIS) technique. The SIS process involved alternating exposures of trimethylaluminum (TMA) and water at 90 °C, conducted utilizing an atom layer deposition (ALD) system (Veeco Savannah S200, USA). During the process, N_2 was empolyed as an inert gas to carry and purge the reactor.

Specifically, thin films of self-assembled BCP coated on silicon substrates were introduced into the ALD reactor. Subsequently, the reactor chamber was purged with a flow of N_2 for 5 min to reduce moisture content and impurities. TMA was used as the metal precursor in the SIS process, and H_2O was regarded as the oxidant. Before starting the infiltration, the temperature of the reactor chamber was thermalized at 90 °C, and the pressure was controlled to less than 20 mTorr. Each SIS cycle was made up of sequential TMA and H_2O pulses. First, TMA was pulsed into the reactor chamber and exposed for 5 min, and then the chamber was purged with N_2 flow for 2 min to remove unreacted precursor and by-products. Second, H_2O was also pulsed into the reactor chamber and exposed for 5 min. Each sample was subjected to the SIS procedure seven times. After the SIS process, the polymer matrix was eradicated through O_2 reactive ion etching (RIE) (Samco RIE-10NR, Japan) for 100 s, leaving AlO_x films that replicated the BCP microdomains on the silicon substrate.

2.4. BCP directed self-assembly by FSA

The contact hole prepatterns on 300 mm silicon wafers were provided by Shanghai Integrated Circuit R&D Center Co., Ltd. (ICRD) (Shanghai, China). Briefly, the guiding patterns of contact hole shrinking, and multiplication required for the graphoepitaxy approach were produced in an organic hard mask. A standard tri-layer stack, consisting of an ArF photoresist layer, a silicon-containing anti-reflective coating (SiARC) layer, and a spin-on carbon (SOC) layer, was deposited onto the 300 mm silicon wafer. To create the hole pattern features, 193 nm immersion (193i) lithography was used on the tri-layer stack of photoresist/SiARC/SOC on the 300 mm silicon wafer. The hole patterns were then dry etched into the SiARC and SOC layers, leading to the creation of the organic guiding pattern cavities characterized by straight profiles. Subsequently, the 300 mm silicon wafers with the contact hole prepatterns were cut into dies with a size of 2.5×3.3 cm^2 to investigate the compatibility of the FSA technique with DSA process. PS-*r*-PMMA (M_n = 8 kg/mol, PS content: 72 mol%) solutions with a concentration of 2.0 wt% in PGMEA were spin-coated onto the dies at 2000 rpm for 60 s. The dies were treated at 220 °C for 5 min in a vacuum oven to chemically graft PS-*r*-PMMA onto the guiding patterns surface, making them more attractive to PS. The dies underwent sonication in a PGMEA bath to eradicate any ungrafted PS-*r*-PMMA, then rinsed with fresh PGMEA and dried using a N_2 flow. PS-*b*-PMMA (M_n = 46.1-*b*-21 kg/mol) solutions with a concentration of 2.0 wt% in PGMEA were spin-coated on top of the grafted PS-*r*-PMMA at 2000 rpm for 60 s. Then, the BCP films were exposed to focused sunlight at a target temperature for ~30 s and cooled down to ambient conditions. To facilitate a direct comparison, the same sample was also subjected to thermal annealing at 225 °C for 5 min in a vacuum oven to induce PS-*b*-PMMA microphase separation.

2.5. Characterization

After annealing, the morphology of BCP thin film was analyzed through field-emission scanning electron microscopy (SEM) (Zeiss GeminiSEM 300, Germany) with an InLens detector. To obtain a better imaging contrast, the BCP films were slightly etched by the O_2 RIE process, followed by Au coating (Cressington 108 Sputter Coater, UK) with 10 mA of discharge current for 5 s in a vacuum. To identify the surface chemistry during the annealing process, X-ray photoelectron spectroscopy (XPS) (Thermo Fisher Scientific ESCALAB Xi^+, USA) analysis was conducted for BCP thin films after both the thermal annealing and the FSA. Thermogravimetric analysis (TGA) (TA Instruments Discovery TGA 5500, USA) was employed to verify the thermal stability of the BCP under ambient air conditions.

2.6. Computation

To quantify the level of order in the self-assembly structures of the BCP, the SEM images were subjected to several image processing steps, including noise reduction, binarization, structure identification, and measurement. The cylindrical domains were identified using contour detection and centroid localization. The critical dimension (CD) of DSA holes was measured by counting the number of pixels. The Delaunay triangulation algorithm was utilized to recognize the hexagonal pattern. To identify the lamellar domains, the binarized images were skeletonized using a morphological operation that reduces the thickness of the features while preserving their topology. The resulting skeleton was then groomed to remove junctions, and the remaining lines were approximated by line segments. This allowed for the identification of the centerlines of the lamellar domains, which were then used to calculate the lamellar pitch and width. The orientational angle θ_{n} is the angle of the long axis of the cylindrical or lamellar domains relative to a reference axis, calculated at a specific position r. The reference axis is usually chosen to be the horizontal direction or the direction of the substrate feature that guides the self-assembly. For the lamellar phase, $n = 2$, and the angle is calculated between the long axis of the lamellar domain and the reference axis. For the hexagonal cylindrical phase, $n = 6$, and the angle is calculated between the direction of the straight line connecting two parallel edges of the hexagonal cylinder and the reference axis. The orientational order parameter $\varphi_n(\boldsymbol{r})$ represents the local orientational order of the cylindrical or lamellar domains at position r. It is calculated as $\varphi_n(r) = \mathrm{e}^{ni\theta_n(r)}$, where n is 2 for the lamellar phase and 6 for the hexagonal cylindrical phase, and $\theta_{\mathrm{n}}(r)$ is the orientational angle at position r. The orientational correlational function $\psi_n(|r|) = \langle \varphi_n^*(r_0)\varphi_n(r_0 + r)\rangle$ is then calculated as the average of the product of the complex conjugate of the orientational order parameter at a reference position r_0 and the orientational order parameter at a position $r_0 + r$. The orientational correlation length ξ_{n} is determined through the fitting of $\psi_n(|r|)$ using an exponential function e^{-r/ξ_n}.

3. Principle of FSA for BCP self-assembly

The Sun, a star at the center of the solar system, continuously radiates energy in the form of electromagnetic waves, such as visible light, ultraviolet light, and infrared radiation. To date, it serves as the primary and crucial source of energy for all life on Earth. On clear days, the power of sunlight on the surface of Earth is about 1000 W/m^2 (i.e., one sun) when the Sun is near the zenith.

As we all know, a biconvex lens is a converging lens that has two outwardly curved surfaces and is capable of focusing light. A collimated beam of light passing through a biconvex lens will converge and focus into a small spot with high energy density, which can result in the heating or even combustion and carbonization of the material at the focal point [7,10]. In this study, the temperature of the light spot can be controlled in the range of 50–600 °C by adjusting the distance between lens and sample, as well as selecting an appropriate biconvex lens. In addition, the surface temperature of the sample can rapidly increase to the desired values within a few seconds after the focused light irradiation. PS-*b*-PMMA is considered a benchmark system in the BCP self-assembly community. It has

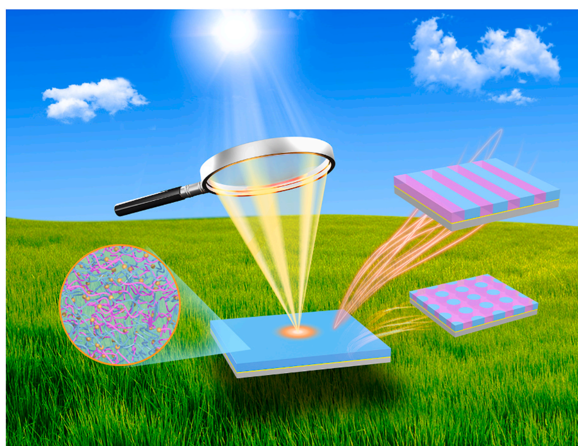

Fig. 1. Schematic diagram of FSA for BCP fast self-assembly.

been extensively used for investigating the mechanism of molecular self-assembly, as well as for industrial applications. It can readily achieve microphase separation and self-assemble to form well-ordered nanostructures at a temperature of 200°–250 °C. Consequently, the self-assembly process can be readily accomplished by exposing PS-*b*-PMMA films to the focused light spot, where sunlight is converged by a biconvex lens. Fig. 1 illustrates a schematic diagram of the fast self-assembly process based upon focused sunlight irradiation. In the FSA technique, normal solar radiation is focused by a biconvex lens, providing high thermal energy that can be directly used to overcome the kinetics barrier during the BCP self-assembly process. More specifically, the silicon substrate absorbs focused sunlight and converts it into intense thermal energy, i.e., photothermal conversion. Because of the high thermal conductivity of silicon ($k = 148\ Wm^{-1}K^{-1}$), the thermal energy is rapidly spread over the entire silicon substrate [32,34]. The PS-*b*-PMMA on the silicon substrate immediately absorb thermal energy for microphase separation. Finally, the PS-*b*-PMMA undergo self-assembly to generate a uniform morphology throughout the entire silicon substrate. In addition, it cannot completely rule out that the PS-*b*-PMMA films may absorb small amounts of sunlight and convert into heat. Nevertheless, the photothermal effect of the PS-*b*-PMMA thin films is insignificant in compared to the silicon substrate. Overall, the FSA technique, like laser annealing [30,32] and flash lamp annealing [34], is a photothermal annealing process.

Interestingly, besides conventional convex lens, Fresnel lenses (including point-focus system and line-focus system) can also converge solar radiation into a point or line with a high thermal energy by means of focusing (transmittance concentrator) or concentrating (reflective concentrator) [10]. Moreover, concave mirrors can also be employed to directly concentrate solar radiation instead of using the conventional biconvex lens. Concave mirrors gather natural solar radiation from a wide area and concentrate it into a small spot or line with high temperature through reflection, similar to concentrating solar power [10]. We believe that the FSA technique will attract attention within the BCP self-assembly communities due to its green, simple process, eco-friendliness, low cost, sustainability, and zero-carbon emissions. In the near future, the FSA technique is expected to realize its full potential with the help of advanced techniques for manipulating sunlight.

4. Results and discussion

4.1. *Temperature of focused sunlight spot*

For the FSA technique applied to BCP self-assembly, the intensity of solar radiation and the size of the focused sunlight spot are the two most critical factors, as they directly determine the final temperature. Generally, the natural solar radiation received by Earth is related to three factors: geographical location, season, and time of day. In this study, we conducted all FSA experiments at the main campus of Fudan University (Shanghai, China), which is located at ~121.5° east longitude and ~31.3° north latitude. As for the other two factors, we measured the sunlight intensity on normal sunny days from 07:00 to 17:00 (Beijing time) during all four seasons using a solar power meter. As depicted in Fig. S1, the direct normal solar irradiation (DNI) can reach 1000 W/m^2 (i.e., one sun) for at least 5 h (from 09:00 to 14:00) on a sunny day in Shanghai, regardless of the season. This provides a sufficiently long-time window to conduct FSA experiments.

Furthermore, we used a solar power meter to directly monitor natural solar radiation on a sunny day at noon, with measurements taken at a rate of one point per second. As shown in Fig. 2A (red line), the measured sunlight intensity was about 1020 W/m^2 (i.e., ~1.02 sun) and displayed excellent stability. Simultaneously, we adjusted the distance between the biconvex lens and the sample to obtain focused light spots of different diameters. The temperature on the sample surface was measured through a digital thermometer, and the results were presented in Fig. 2B (red dots). As the diameter of the focused spot decreased, the temperature of the sample surface increased. Specifically, by adjusting the distance between the biconvex lens and the sample, the ~1020 W/m^2 sunlight passing through the 18 cm biconvex lens produces the focused light spot diameters of approximately 2.0, 1.5, 1.0, and 0.5 on sample surface.

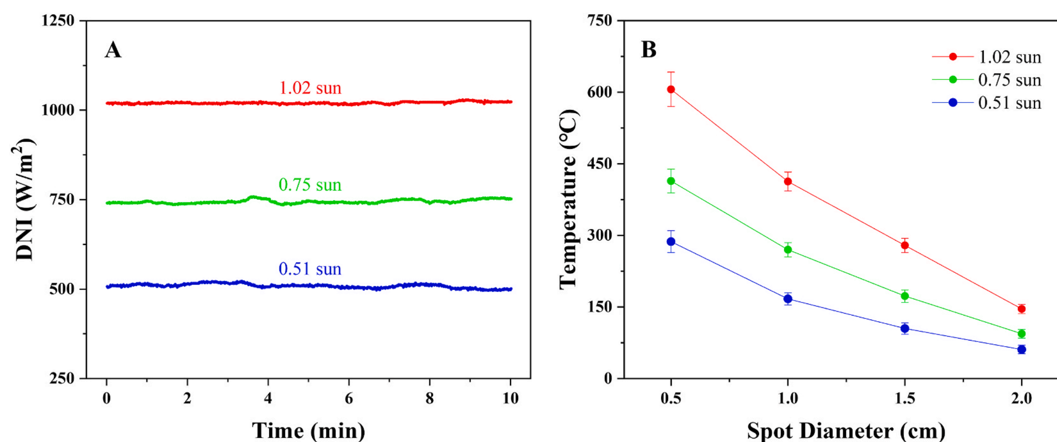

Fig. 2. Under different sunlight intensity, (A) temporal variations of the DNI and (B) the relationship between the temperature and the spot diameter of focused sunlight.

The corresponding temperatures were about 146 ± 10, 279 ± 15, 413 ± 20, and 606 ± 36 °C, respectively. Therefore, the PS-*b*-PMMA self-assembly can be readily achieved by the FSA technique.

Additionally, it is noteworthy that the intensity of sunlight reaching the ground does not remain constant at around 1000 W/m^2 throughout the day, as displayed in Fig. S1. Therefore, it is essential to investigate the focused light spot's temperature on the sample surface under different sunlight intensities. Here, we selected two sunlight intensities for analysis, which were ~750 W/m^2 (i.e., ~0.75 sun) and ~510 W/m^2 (i.e., ~0.51 sun). In Fig. 2A, the green and blue lines present the DNI against time at about 0.75 sun and 0.51 sun, respectively. Both intensities exhibit good stability over time. Moreover, the corresponding temperatures of focused light spots with different diameters were investigated at these two intensities. As shown in Fig. 2B (green dots), when the DNI was about 0.75 sun, the temperatures of the focused light spots with diameters of about 2.0, 1.5, 1.0, and 0.5 cm were about 94 ± 9, 173 ± 13, 270 ± 15, and 414 ± 25 °C, respectively. When the DNI was about 0.51 sun, the temperatures of the focused sunlight spots with different diameters were about 61 ± 9, 105 ± 12, 167 ± 13, and 284 ± 23 °C, corresponding to the diameters of about 2.0 cm, 1.5 cm, 1.0 cm, and 0.5 cm, respectively, as depicted in Fig. 2B (blue dots). These data demonstrate that the FSA technique for PS-*b*-PMMA self-assembly is effective across a range of sunlight intensities, from 0.5 to 1.0 sun. It should be noted that all FSA experiments in this study were conducted at a DNI of approximately 1.0 sun, which corresponds to around 1000 W/m^2.

4.2. FSA for PS-b-PMMA self-assembly

BCP refers to a class of copolymers that made up of two or more chemically different homopolymer blocks joined together through covalent bonds [21]. Among them, linear A-*block*-B diblock copolymers are the simplest and most commonly studied molecules within the BCP family. Under appropriate conditions, the phase separation between blocks A and B occurs on the micro scale instead of the macro level because of the covalent linkage between the two blocks, and ordered nanostructures such as cylinders, lamellae, gyroids, and spheres are formed, that is, BCP self-assembly [20,21].

PS-*b*-PMMA is among the most commonly investigated materials in the community of BCP self-assembly [20]. Because the surface energy difference between the PS and PMMA blocks is modest across a wide temperature range. Besides, in PS-*b*-PMMA, the etching selectivity ratio between PS and PMMA blocks can reach 1:2. As a result, the domains' orientation of PS-*b*-PMMA on substrates may be easily controlled. To validate the effectiveness of the FSA technique for BCP self-assembly, two types of PS-*b*-PMMA molecules are employed in this study. The first type is a symmetric PS-*b*-PMMA (M_n = 31-*b*-33 kg/mol) and the second type is an asymmetric

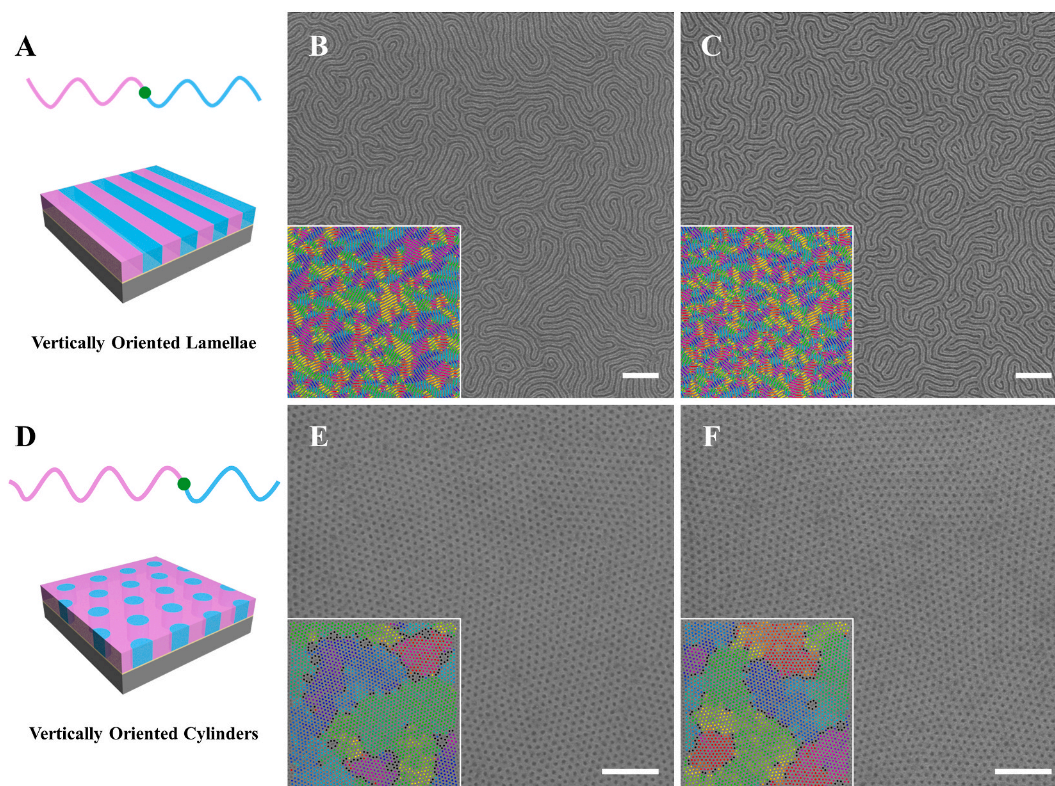

Fig. 3. Schematic diagram of vertically oriented (A) lamellae and (D) cylinders of PS-*b*-PMMA structures. SEM images of the microphase separation morphology of PS-*b*-PMMA (M_n = 31-*b*-33 kg/mol) induced by (B) FSA process and (C) conventional thermal annealing process. SEM images of the microphase separation morphology of PS-*b*-PMMA (M_n = 37-*b*-16.8 kg/mol) induced by (E) FSA process and (F) conventional thermal annealing process. All scale bars are 200 nm. The inset illustrates the orientation mappings of self-assembled nanostructures.

PS-*b*-PMMA (M_n = 37-*b*-16.8 kg/mol). After annealing process, the symmetric PS-*b*-PMMA sample forms vertically oriented lamellae on a neutral surface, as depicted in Fig. 3A. In contrast, the asymmetric PS-*b*-PMMA sample produces vertically oriented cylinders on a neutral surface, where PMMA cylinders are inserted in the PS matrix, as illustrated in Fig. 3D. The self-assembled morphologies of PS-*b*-PMMA were analyzed using SEM. Fig. 3B and S2 present the self-assembled morphology of PS-*b*-PMMA (M_n = 31-*b*-33 kg/mol) induced by the FSA method. In this experiment, the temperature is 250 ± 15 °C and the processing time is about 30 s. The result clearly shows that PS-*b*-PMMA form perpendicularly oriented fingerprint-like structures on neutral polymer brushes modified silicon substrates after the FSA process. For comparison, conventional thermal annealing was also employed to drive PS-*b*-PMMA self-assembly. Specifically, the same PS-*b*-PMMA samples were placed in a vacuum oven at 250 °C for 5 min to facilitate microphase separation. Fig. 3C and S3 display the microphase-separated morphology of PS-*b*-PMMA induced through the conventional thermal annealing process. The similar vertically oriented microdomains with fingerprint-like structures are obtained. These results directly demonstrate that the FSA technique is capable of inducing BCP microphase separation, like conventional thermal annealing.

To gain a better understanding of pattern ordering, the SEM images were quantitatively characterized by a home-made image analysis technique. The orientation mappings of PS-*b*-PMMA self-assembled nanostructures through the FSA and conventional thermal annealing processes are shown in the insets of Fig. 3B and C, respectively. Detailed definitions of the various line renderings are displayed in Figs. S2 and S3. The data indicate that the BCP self-assembled nanostructures induced by FSA exhibit greater ordering than those obtained by conventional thermal annealing. More importantly, the orientational correlation length (ξ) of fingerprint-like

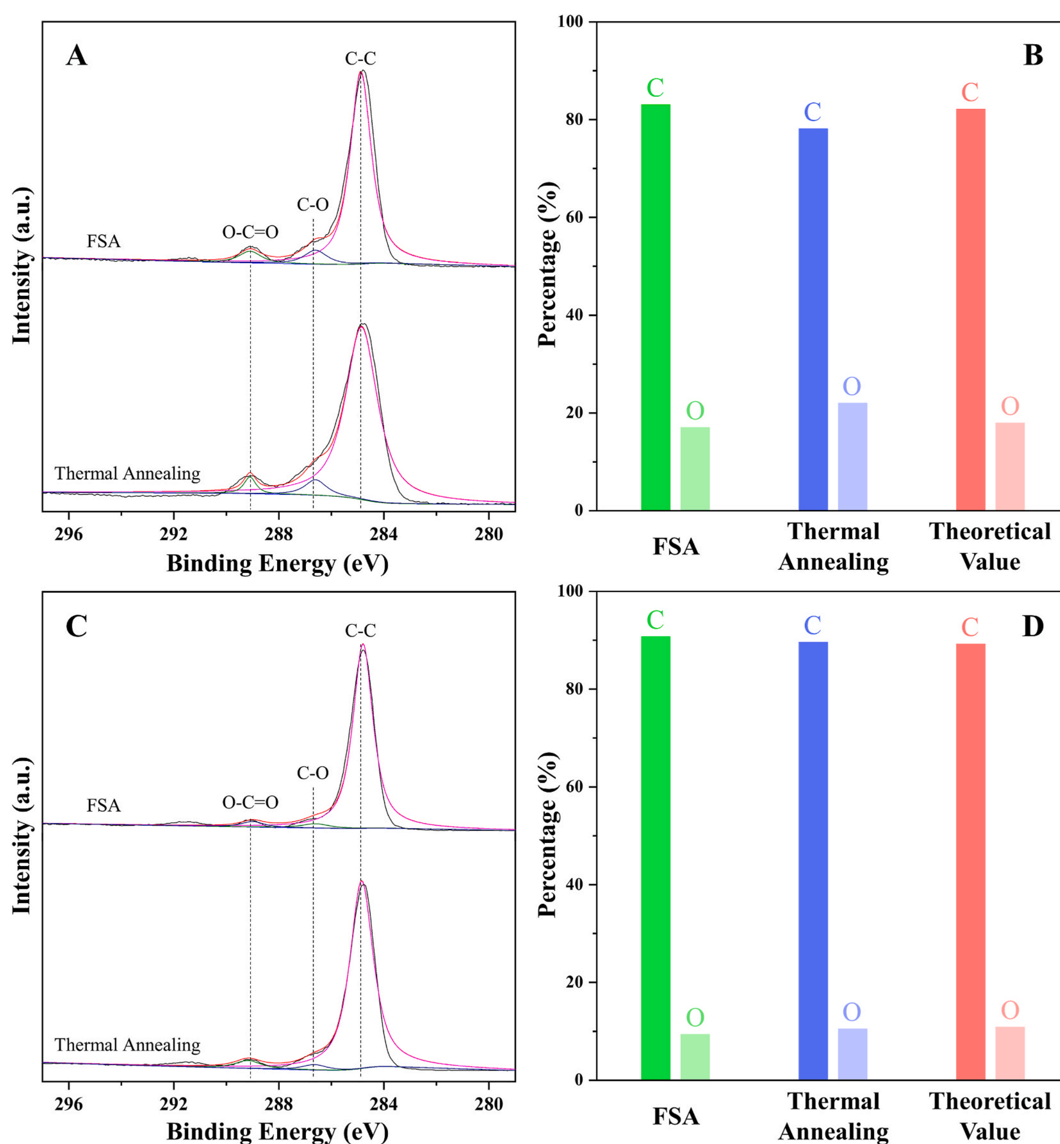

Fig. 4. (A) XPS C 1s spectra and (B) carbon and oxygen contents of PS-*b*-PMMA (M_n = 31-*b*-33 kg/mol) thin films after various annealing processes. (C) XPS C 1s spectra and (D) carbon and oxygen contents of PS-*b*-PMMA (M_n = 37-*b*-16.8 kg/mol) thin films after various annealing processes.

nanostructures in Fig. 3B and C were also determined. Fig. S2 shows that the ξ of the FSA-induced PS-*b*-PMMA microphase-separation pattern is about 71 nm. In contrast, Fig. S3 displays that the ξ value is about 48 nm for conventional thermal annealing. It is possible that the discrepancies in correlation length between the FSA-induced and conventionally thermally annealed PS-*b*-PMMA microphase-separation patterns could be attributed to differences in the annealing parameters such as temperature, surrounding humidity, ambient atmosphere, etc. It should be noted that although the FSA technique also belongs to thermal annealing in essence. After all, the FSA process is performed under atmospheric conditions, while traditional thermal annealing is conducted under vacuum. Further investigation is necessary to draw a definitive conclusion.

Likewise, the self-assembly behavior of PS-*b*-PMMA (M_n = 37-*b*-16.8 kg/mol) on neutral polymer brushes modified silicon substrates was compared between the FSA and the conventional thermal annealing. Fig. 3E and S4 present that the cylinder-forming PS-*b*-PMMA sample forms hexagonal arrays of perpendicular cylinders with PMMA cylinders embedded in the PS matrix *via* the FSA. The Delaunay triangulation algorithm was used to quantitatively characterize the hexagonal pattern. The center-to-center distance of the hexagonal array was measured to be 28.2 ± 2.9 nm, and the CD of the PMMA cylinders was 12.3 ± 1.1 nm. In addition, the orientational orders of the hexagonal array were also obtained as colored in the inset of Fig. 3E, displaying a high level of order. The rendering of the various hexagons is defined in detail in Fig. S4. The ξ of the hexagonal array was precisely measured to be about 198 nm (Fig. S4). For comparison, the same PS-*b*-PMMA samples were subjected to conventional thermal annealing in a vacuum oven at 220 °C for 15 min to induce microphase separation. Fig. 3F and S5 also exhibit hexagonal arrays with PMMA cylinders insert in the PS matrix. The self-assembled morphologies are similar to those in Fig. 3E. The hexagonal array in Fig. 3F was quantitatively characterized with a center-to-center distance of 28.3 ± 2.6 nm and a CD of 12.3 ± 1.2 nm for the PMMA cylinders, which are consistent with the findings in Fig. 3E. The inset of Fig. 3F is orientation mapping of self-assembled nanostructures through the thermal annealing process, showing a good ordering, too. The definitions of the rendering of various hexagons are displayed in Fig. S5. The hexagonal array's ξ was calculated to be about 210 nm (Fig. S5), similar to the data in Fig. 3E. The results further confirm that the FSA displays the same capacity to promote PS-*b*-PMMA microphase separation as conventional thermal annealing.

It is worth noting that polymer degradation may need to be particularly concerned in the use of the FSA technique for BCP self-assembly. Since the FSA technique involves a high-temperature process that utilizes focused solar irradiation under atmospheric conditions. To clarify this issue, we conducted both XPS and TGA analyses to study the physical as well as chemical characteristics of PS-*b*-PMMA. First, PS-*b*-PMMA on substrates were analyzed by XPS after the annealing process, which included both thermal annealing and FSA. Fig. 4A presents the XPS C 1s spectra of PS-*b*-PMMA (M_n = 31-*b*-33 kg/mol) thin films after the FSA process and thermal annealing process, respectively. The two XPS C 1s spectra display exhibit similar features, and the relative intensities of C–C peak (~284.8 eV), C–O peak (~286.6 eV), and O–C=O peak (~288.9 eV) are nearly identical in both spectra. In addition, based upon the survey XPS spectra (Fig. S6), the percentages of carbon and oxygen content in annealed PS-*b*-PMMA may be accurately obtained. After the FSA process, the self-assembled PS-*b*-PMMA contained 83.02 % carbon and 16.98 % oxygen (Fig. 4B, green histogram). The thermally annealed PS-*b*-PMMA consisted of 78.07 % carbon and 21.93 % oxygen (Fig. 4B, blue histogram). For comparison with XPS data, we assume that the hydrogen content is ignored. The theoretical carbon and oxygen contents of PS-*b*-PMMA with molecular weights of 31-*b*-33 kg/mol are 82.09 % and 17.91 % (Fig. 4B, cherry histogram), respectively. The XPS analysis of 31-*b*-33 kg/mol PS-*b*-PMMA after the FSA confirms that thermal degradation is insignificant. Similarly, to identify the surface chemistry during the annealing process, XPS analysis was also used to characterize PS-*b*-PMMA (M_n = 37-*b*-16.8 kg/mol) thin films after FSA and thermal annealing process, respectively, as presented in Fig. 4C and S6. The shapes and relative intensities of peaks in the two XPS C 1s spectra are analogous without any noticeable difference. According to the survey XPS spectra in Fig. S6, the carbon content is 90.67 % and oxygen content is 9.33 % for self-assembled PS-*b*-PMMA after the FSA process (Fig. 4D, green histogram). In contrast, the thermally annealed PS-*b*-PMMA comprised 89.54 % carbon and 10.46 % oxygen (Fig. 4D, blue histogram). To better compare with the XPS data, assumedly ignoring the hydrogen content, the theoretical carbon and oxygen contents of the 37-*b*-16.8 kg/mol PS-*b*-PMMA are 89.16 % and 10.84 % (Fig. 4D, cherry histogram), respectively. Taken together, these results also verify that the thermal degradation of cylinder-forming PS-*b*-PMMA with molecular weights of 37-*b*-16.8 kg/mol by the FSA process is insignificant under our experimental conditions. Second, the thermal stability of two types of PS-*b*-PMMA powders are investigated by TGA under air condition with heating from 30 to 800 °C at 10 °C/min, as illustrated in Fig. S7. The results imply that the weight of PS-*b*-PMMA remains above 95 % at around 250–270 °C, i.e., less than 5 % weight loss, confirming that polymer degradation is insignificant in the FSA experiments. It is worthwhile to mention that the self-assembly behavior of PS-*b*-PMMA using the FSA method can be completed in ~30 s. In addition, many studies have shown that the annealing of PS-*b*-PMMA can be done at around 250 °C for several minutes under ambient conditions [36–39]. Taken together, all these facts clearly evidence that thermal degradation during the FSA process is negligible.

There is another issue that needs to be clarified. FSA technique is a method for BCP microphase separation at second timescales, whereas conventional thermal annealing takes several minutes or even hours. Does FSA-induced BCP self-assembly produce the expected perpendicular structures? To address this issue, we examined cross-sectional SEM images of the FSA-induced BCP nanostructures. Due to the soft nature of PS-*b*-PMMA, direct characterization of its cross-sectional morphologies by SEM is extremely challenging. Therefore, we employed SIS technology to synthesize AlO_x nanostructures within the PMMA domain, which allowed for the visualization of clear and accurate three-dimensional morphologies. The SIS procedure was conducted in an ALD reactor. During the SIS, H_2O and TMA were utilized as oxidants and metal precursors, respectively. The SIS process temperature was selected to be slightly below the glass-transition temperature (T_g) of the PS-*b*-PMMA to allow for easy diffusion of the reactants into the PMMA domains without compromising the integrity of the constructed nanostructure. Fig. S8 presents top-view and 45° tilted SEM images of the AlO_x fingerprint-like structures produced by infiltration of TMA and H_2O into PS-*b*-PMMA (M_n = 31-*b*-33 kg/mol) with vertically oriented microdomains, followed by removal of the polymeric phase using an O_2 RIE process. The top-view SEM confirms that the morphology of the AlO_x nanostructures completely mimics the PMMA component's morphology in the initial BCP templates. Of

particular importance, the 45° tilted SEM image displays that the AlO_x nanostructures stand vertically on the silicon substrate, indicating that the FSA-induced PS-*b*-PMMA microphase separation results in the top-bottom penetrating stereostructures. Fig. S9 presents top-view and 45° tilted SEM images of the AlO_x dot arrays generated through infiltration of TMA and H_2O into PS-*b*-PMMA (M_n = 37-*b*-16.8 kg/mol) films. Out-of-plane hexagonally packed PMMA cylinders are inserted in the PS matrix, and then the polymeric phase is eradicated using an O_2 RIE process. The top-view SEM image reveals that the AlO_x dots are uniformly distributed over a large area, implying that the SIS process effectively converts the PMMA cylinders included in the PS matrix into AlO_x cylinders. Furthermore, the 45° tilted SEM image shows that each AlO_x cylinder stands upright on the silicon substrate, verifying that the microphase separation of cylinder-forming PS-*b*-PMMA induced through FSA also achieves the expected top-bottom penetrating stereostructures. These findings show that the FSA-induced BCP self-assembly can also achieve the top-bottom penetrating stereostructures as conventional thermal annealing.

Overall, compared to conventional thermal annealing, due to the direct use of primary energy (i.e., solar energy) and the BCP self-assembly process carried out in air, our developed FSA technique presents several advantages, such as greatly reducing process time and saving energy. These results strongly suggest that the FSA technique can be used as a complementary method to conventional thermal annealing for promoting PS-*b*-PMMA microphase separation into ordered nanostructures.

4.3. *Influence of annealing time*

To further understand how BCP ordering evolves over time throughout the FSA method, we conducted self-assembly experiments of

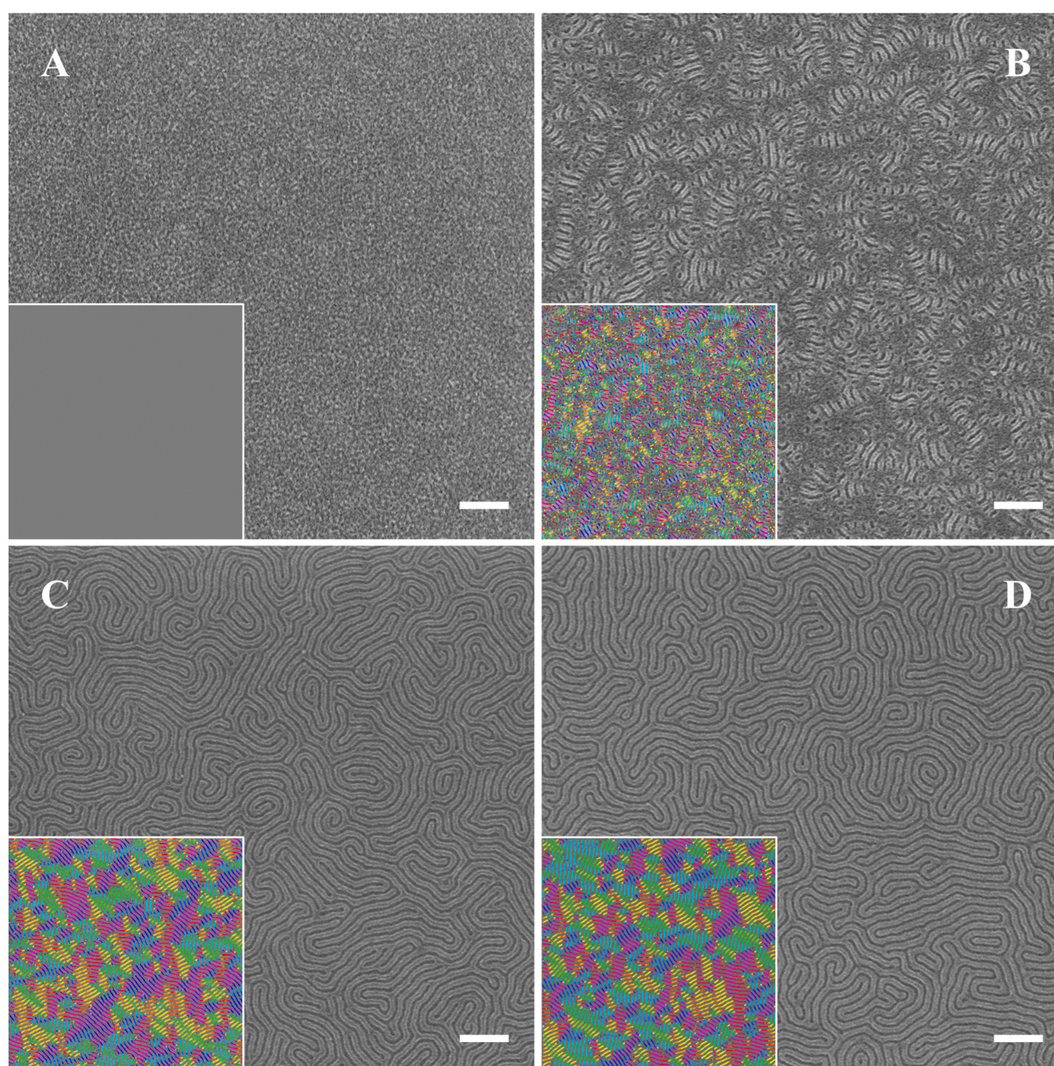

Fig. 5. Influence of annealing time over the BCP self-assembly. SEM images of the lamella-forming PS-*b*-PMMA (M_n = 31-*b*-33 kg/mol) self-assembled structures by the FSA process at (A) 5 s, (B) 15 s, (C) 30 s, and (D) 45 s. All scale bars are 200 nm. The inset illustrates the orientation mappings of self-assembled nanostructures.

PS-*b*-PMMA (M_n = 31-*b*-33 kg/mol) thin films at various annealing time while keeping all the other process parameters fixed. Fig. 5 depicts the morphological evolution of PS-*b*-PMMA films using the FSA technique at varying annealing times. After annealing for 5 s, the PS-*b*-PMMA films did not exhibit any discernible ordered morphologies (Fig. 5A) and the corresponding orientation mappings is blank, implying that the microphase separation process does not occur notably. This may be attributed to the fact that the annealing time of 5 s is insufficient. The temperature may have just reached the desired annealing temperature, but the annealing process had already ended by that time. With the annealing time extended to 15 s, as depicted in Fig. 5B, the morphologies display very short-range ordered structures with numerous defects, i.e., worm-like structures, which were notably different from those observed in Fig. 5A. Finally, upon annealing for more than 30 s, a vertical orientation of lamellar domains with fingerprint-like nanostructures (Fig. 5C) was observed. In particular, as the annealing time was further increased to 45 s, the PS-*b*-PMMA morphologies (Fig. 5D) remain consistent with those observed in Fig. 5C. This indicates that an annealing time of 30 s at 250 ± 15 °C is adequate induce the formation of vertically oriented nanostructures.

4.4. FSA for PS-r-PMMA grafting

In general, silicon substrates feature a native oxide layer that exhibits a preferential interaction with the hydrophilic PMMA block rather than the hydrophobic PS block in PS-*b*-PMMA. Consequently, lamella- (or cylinder-) forming PS-*b*-PMMA will generate parallel oriented lamellar (or cylindrical) domains on this substrate. To achieve perpendicularly oriented domains in PS-*b*-PMMA films, many efforts have been devoted to modifying the silicon substrate with self-assembled monolayers [40], polystyrene (PS) homopolymer [37], random copolymer [24,25,39], and block cooligomers [41]. Among these, the most widely used approach is treating the silicon substrate with a random copolymer brush, such as PS-*r*-PMMA. The PS-*r*-PMMA is grafted onto the substrate surface by a condensation

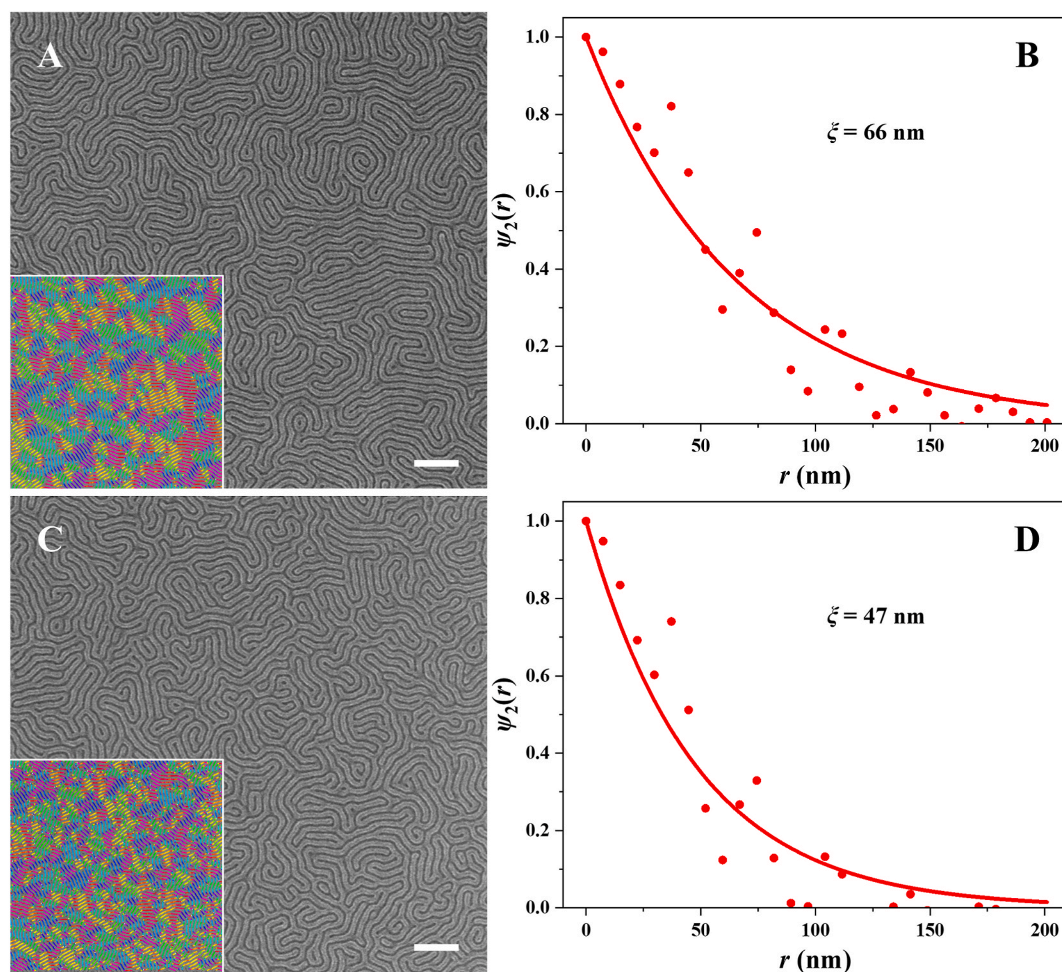

Fig. 6. SEM images of vertically oriented lamellae of PS-*b*-PMMA (M_n = 31-*b*-33 kg/mol) structures by (A) FSA process and (C) conventional thermal annealing process, the scale bars are 200 nm. The inset illustrates the orientation mappings of self-assembled nanostructures. (B) The calculation of the bond-order correlation function, $\psi_2(r)$, is derived from SEM image A. (D) The calculation of the bond-order correlation function, $\psi_2(r)$, is derived from SEM image C.

reaction, producing a neutral molecular layer [25]. The process of PS-*r*-PMMA brush grafting typically takes from a few minutes to several days in a vacuum oven at 160–300 °C, analogous to thermal annealing for PS-*b*-PMMA self-assembly. Therefore, we also employed the FSA method to graft the PS-*r*-PMMA onto the silicon substrates, instead of the conventional grafting method (i.e., thermal treatment in a vacuum oven), for the PS-*b*-PMMA self-assembly.

First of all, the solutions of PS-*r*-PMMA (M_n = 40.7 kg/mol, PS content: 58 mol%) were spin-coated onto piranha-clean silicon substrates and subsequently exposed to a focused light spot with a temperature 250 ± 15 °C for 60 s. Second, the substrates were sonicated in warm toluene to eradicate any ungrafted PS-*r*-PMMA polymer and rinsed with fresh toluene. Third, the PS-*b*-PMMA (M_n = 31-*b*-33 kg/mol) solutions were spin-coated onto PS-*r*-PMMA modified silicon substrates to form ~38 nm thin films. Finally, the PS-*b*-PMMA thin films were treated by the FSA process and conventional thermal annealing process, respectively, to promote microphase separation and attain an equilibrium morphology. As shown in Fig. 6A, vertical orientation of lamellar domains with fingerprint-like nanostructures is achieved through the FSA process. Fig. 6B displays the calculation of the bond-order correlation function, $\psi_2(r)$, derived from the SEM image. Based upon the $\psi_2(r)$, the ξ of the PS-*b*-PMMA microphase-separation pattern is determined to be about 66 nm. For comparison, the same PS-*b*-PMMA samples were placed in a vacuum oven at 250 °C for 5 min to realize their microphase separation. Fig. 6C also presents the vertically oriented lamellae of PS-*b*-PMMA nanostructures, while its ξ was determined to be about 47 nm (Fig. 6D), which is shorter than that of Fig. 6A. The results demonstrate the feasibility of grafting PS-*r*-PMMA polymer brushes onto silicon substrates using the FSA technique.

Meanwhile, we also compared Fig. 6A with Fig. 3B, where PS-*r*-PMMA polymer brushes were grafted onto silicon substrates using the FSA method and conventional thermal treatment, respectively; while the annealing procedure for PS-*b*-PMMA remained the same, i.e., the FSA process. In these SEM images, the morphology and ξ of the PS-*b*-PMMA self-assembled pattern maintain analogous without notable differences. Similarly, Figs. 6C and 3C were also compared, where PS-*r*-PMMA polymer brushes were grafted onto silicon substrates using the FSA approach and conventional thermal treatment, respectively. The annealing process for PS-*b*-PMMA in both cases was conventional thermal annealing. The two SEM images show similar morphologies and ξ for the PS-*b*-PMMA self-assembled patterns. Taken together, these results directly and clearly demonstrate that the FSA method can also be used for grafting PS-*r*-PMMA polymer brushes onto silicon substrates with grafting efficiencies comparable to that of conventional thermal treatment.

Consequently, the developed FSA technique may be employed not only for PS-*b*-PMMA self-assembly but also for grafting PS-*r*-PMMA onto silicon substrates. Actually, all polymer brushes grafted by conventional thermal treatment could also be achieved with FSA method, e.g., grafting PS homopolymers, various random copolymers, block cooligomers and so on.

4.5. FSA for PS-b-PMMA directed self-assembly

Currently, considerable efforts are being made to control the registration and orientation of microphase-separated BCP domains. Numerous techniques, such as graphoepitaxy [42,43], chemical prepatterning [40,44,45], shear alignment [46,47], electric field alignment [48], boundary-directed epitaxy [49], laser-induced alignment [30–32], have been employed to guide the assembling of BCP films. Here, the FSA technique was assessed to verify its compatibility with the DSA process in the applications such as contact hole shrinking and contact hole multiplication.

Contact hole patterning using DSA is one of the most promising applications in semiconductor nanodevice manufacturing. The reason is that the DSA technique offers an efficient method for creating high-resolution contact holes with critical dimensions (CDs)

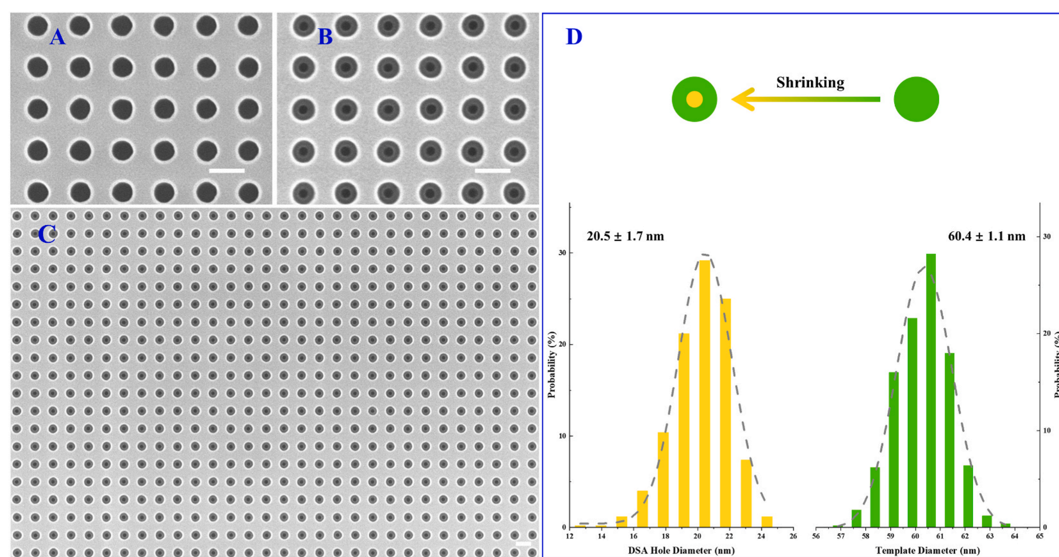

Fig. 7. (A) SEM image of contact hole shrinking templates at 100 k magnification. SEM images of singlet DSA hole per template at (B) 100 k and (C) 30 k magnifications. All scale bars are 100 nm. (D) The CD of the singlet DSA hole and circular guiding templates.

smaller than 30 nm and provides improved CD uniformity compared to conventional lithography. The graphoepitaxy DSA technique may be employed to generate single or multiple uniform contact holes within a pre-pattern template, surpassing the resolution limit of the optical exposure instrument. We employed the same graphite epitaxy flow as described in the literature for DSA hole patterning with cylinder-forming BCP [50]. Briefly, a standard tri-layer, consisting of an ArF photoresist layer, SiARC layer and SOC layer, was prepared on 300 mm substrate wafer. 193i lithography was used to define the prepattern templates for contact holes in the ArF photoresist. The hole prepatterns in the photoresist was obtained by a developing process. Then, a dry etching process was employed to transfer the hole prepatterns from the photoresist to the SiARC and SOC layers. The organic guide pattern cavities with straight profiles were formed after removal of the residual photoresist. PS-*r*-PMMA was grafted onto the surface of the guiding pattern cavities to serve as a neutral layer. PS-*b*-PMMA materials were then spin-coated onto the prepatterned template. The sample was exposed to focused sunlight at 250 ± 15 °C for ∼30 s under ambient conditions to drive PS-*b*-PMMA self-assembly. After the FSA process, the DSA hole patterns were slightly etched using O_2 RIE process to improve imaging contrast. Finally, the morphologies of the DSA hole patterns were characterized by SEM using an InLens detector.

For contact hole shrinking, a well-defined guiding prepattern template was used, which consisted of an array of circular holes with a depth of ∼200 nm, a diameter of ∼60 nm, and a pitch of ∼120 nm, as depicted in Fig. 7A. The template has a very vertical sidewall profile, as verified by a focused ion beam-transmission electron microscopy (FIB-TEM) image, with an etch angle of approximately 88.7° (Fig. S10). This vertical sidewall profile is beneficial for PS-*b*-PMMA molecule self-assembly within the deep cavities.

Fig. 7B shows the morphologies of the self-organized cylindrical phase PS-*b*-PMMA (M_n = 46.1-*b*-21 kg/mol) molecules within the guiding prepattern templates through the FSA method. The PS-*b*-PMMA assembly nanopattern successfully formed a singlet DSA hole in each circular guiding hole. Fig. 7C displays a low-magnification SEM image of the DSA hole within the guiding templates. It presents 600 singlet DSA holes with a very uniform morphology, all of which are opened, showing an excellent HOY of 100 %. Besides, we observed 1598 singlet DSA holes in a region of 5.6 × 4.0 μm^2, and all DSA holes were also opened (Fig. S11), suggesting the robust capability of the FSA technique. To obtain in-depth information about these DSA holes, we conducted precise quantitative analysis on the singlet DSA holes' features using our home-made CD measurement software, as presented in Fig. 7D. The average CD of the singlet DSA hole was determined to be 20.5 ± 1.7 nm, indicating that the hole prepatterns of ∼60.4 nm could be shrunk uniformly to DSA hole patterns of ∼20.5 nm with a HOY of 100 % over a large area. The results demonstrate that the FSA technique is compatible with the DSA process for contact hole shrinking and can significantly increase the pattern resolution of contact holes by up to 3 times. For comparison, the same sample underwent thermal annealing at 225 °C for 5 min in a vacuum oven to induce microphase separation of PS-*b*-PMMA within the same guiding prepattern template. Fig. S12 is the SEM images at the same magnification of morphologies of the singlet DSA holes prepared by FSA and conventional thermal annealing, respectively. They exhibit similar features: the CD of singlet DSA holes is about 20.5 nm, and the HOY is 100 %. Therefore, the FSA technique can serve as a complementary method to conventional thermal annealing for the shrinking of contact holes.

The compatibility of the DSA process with FSA technique was also verified in the application of contact hole multiplication. Fig. 8A presents the well-defined elliptical guiding prepattern templates. In the *x*-direction, the template's CD and pitch are ∼72 and ∼132 nm, respectively; while in the *y*-direction, its CD and pitch are ∼124 and ∼200 nm, respectively. After the FSA process, the self-assembled nanopatterns of the well-ordered doublet DSA holes were generated in the elliptical guiding templates, as shown in Fig. 8B. The low magnification SEM image in Fig. 8C presents 324 elliptical guiding holes, each of which forms doublet DSA holes with a very uniform morphology, indicating an excellent HOY of 100 %. The lower magnification SEM image (Fig. S13) exhibits 860

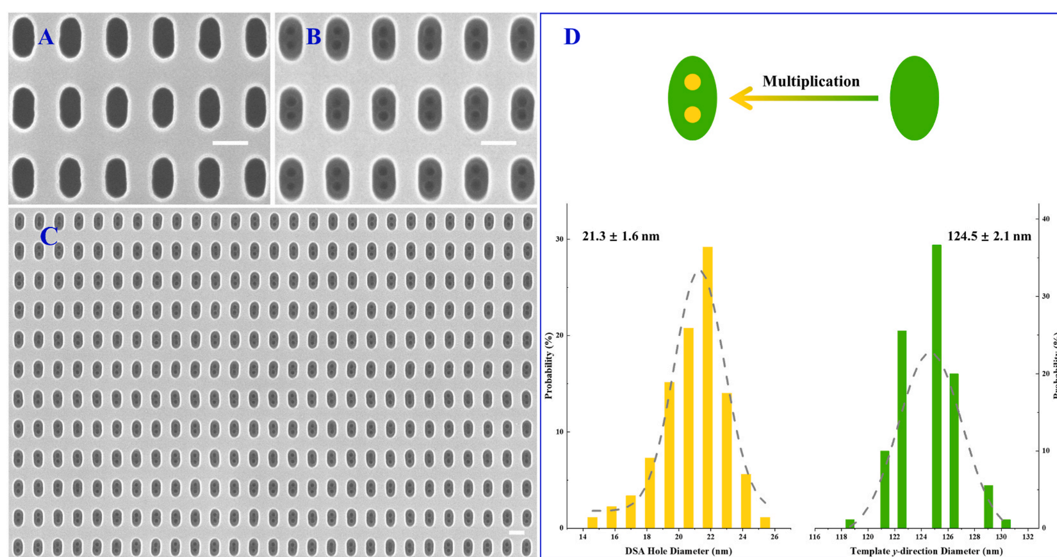

Fig. 8. (A) SEM image of contact hole multiplication templates at 100 k magnification. SEM images of doublet DSA hole per template at (B) 100 k and (C) 30 k magnifications. All scale bars are 100 nm. (D) The CD of the doublet DSA hole and elliptical guiding templates in *y*-direction.

elliptical guiding holes in a region of 5.6 × 4.0 μm^2, where each template produces uniform CD's doublet DSA holes with a 100 % HOY. To better analyze DSA holes, the home-made CD measurement software was also employed for precise quantitative measurements of the CD of doublet DSA holes as well as the center-to-center distance between doublet DSA holes. Fig. 8D displays that the average CD of the doublet DSA holes has been measured to be 21.3 ± 1.7 nm, and the elliptical template's CD in *y*-direction has been calculated to be ~124.5 nm. Meanwhile, the center-to-center distance of the doublet DSA holes is determined to be ~40 nm, closely aligning with the PS-*b*-PMMA material's bulk period of ~37.5 nm. The results consistently confirm that the FSA method can be combined with DSA process for contact hole multiplication. Besides, the same sample was also subjected to thermal annealing at 225 °C for 5 min in a vacuum oven to drive PS-*b*-PMMA self-assembly in the same elliptical guiding prepattern template. Fig. S14 presents SEM images at the same magnification of morphologies of doublet DSA holes generated through the FSA technique and conventional thermal annealing, respectively. The DSA holes produced by both methods exhibit similar characteristics with a CD of ~21.3 nm and a HOY of 100 %. These results suggest that the FSA technique is well compatible with DSA process, similar to conventional thermal annealing.

Noteworthily, XPS analysis and TGA were also conducted to investigate the issue of the PS-*b*-PMMA (M_n = 46.1-*b*-21 kg/mol) polymer degradation. 2.0 wt% PS-*b*-PMMA solutions were prepared in PGMEA and spin-coated onto silicon substrates to generate uniform thin films. The BCP thin films were then treated by FSA and thermal annealing, respectively. Fig. S15 shows the XPS results of PS-*b*-PMMA after two different annealing processes, namely FSA and thermal annealing. All of the XPS C 1s spectra after annealing process maintain analogous without any variation. Particularly, the carbon and oxygen contents can be accurately determined based upon the survey XPS spectra. After the FSA process, the BCP thin films contained 87.89 % carbon and 12.11 % oxygen; whereas after the thermal annealing process, the carbon content was 89.75 % and oxygen content was 10.25 %. To compare with the XPS data, we ignore the hydrogen content, and the theoretical carbon and oxygen contents of PS-*b*-PMMA are 89.14 % and 10.86 %, respectively. Comparing the XPS data and theoretical values (Fig. S15), it can be deduced that thermal degradation is insignificant during the FSA process. Furthermore, the thermal stability of PS-*b*-PMMA powders was investigated by TGA under air atmosphere with heating from 30 to 800 °C at 10 °C/min (Fig. S16). The weight loss of PS-*b*-PMMA less than 4 % at around 250–270 °C, inducting that the polymer degradation could be ignored in the FSA experiments.

In short, the FSA technique, as a complementary approach to conventional thermal annealing, has been shown to be well compatible with the DSA process. For instance, using the FSA process, BCP molecules can self-assemble in guide templates to form uniform ~21 nm stable DSA hole patterns with a 100 % HOY in the application of contact hole patterning. The potential of this approach can be further enhanced in the near future by leveraging more advanced techniques for manipulating sunlight, ultimately leading to practical applications.

5. Conclusions

In this work, we have successfully developed a novel, green, facile, and electricity-free FSA method for fast self-assembly of BCP. The FSA's principle is to utilize a biconvex lens to converge solar radiation into a high temperature spot, which is directly employed to overcome the kinetics barrier in the microphase separation of BCP. Using the FSA technique, PS-*b*-PMMA thin films on polymer brush modified silicon substrates were successfully self-assembled into highly ordered nanostructures with a vertical orientation at timescales of seconds. Besides, the FSA method was also used for grafting neutral polymer brushes onto silicon substrates. More importantly, the compatibility of the FSA technique with the DSA process has been also confirmed in the applications of contact hole patterning. The results clearly demonstrated that the FSA method can act as a complement to conventional thermal annealing for the ordered self-assembly of PS-*b*-PMMA films. Due to the direct use of green, cost-free, pollution-free, and inexhaustible primary energy (i.e., solar energy), the FSA technique provides a promising alternative route for BCP lithography and also serves as an inspiration for light-to-heat conversion applications in other areas such as materials synthesis and energy utilization and takes a significant step forward in energy conservation and emission reduction, particularly in achieving carbon neutrality.

Data availability

Data will be made available on request.

CRediT authorship contribution statement

Xiao-Hua Hu: Writing – review & editing, Writing – original draft, Visualization, Validation, Supervision, Resources, Project administration, Methodology, Investigation, Formal analysis, Data curation, Conceptualization. **Rui Zhang:** Visualization, Validation, Methodology, Investigation, Formal analysis, Data curation. **Xiaohui Zhang:** Visualization, Validation, Software, Methodology, Investigation, Formal analysis, Data curation. **Zhiyong Wu:** Software, Methodology, Investigation, Formal analysis, Data curation. **Jing Zhou:** Methodology, Formal analysis, Data curation. **Weihua Li:** Writing – review & editing, Supervision, Software, Resources, Project administration, Methodology, Funding acquisition, Conceptualization. **Shisheng Xiong:** Writing – review & editing, Supervision, Resources, Project administration, Methodology, Funding acquisition, Conceptualization.

Declaration of competing interest

The authors declare that they have no known competing financial interests or personal relationships that could have appeared to influence the work reported in this paper.

Acknowledgements

S.X. thanks Ms. Manhua Shen (ICRD, China) for providing the DSA guiding templates. S.X. thanks Prof. Shengxiang Ji (Changchun Institute of Applied Chemistry, Chinese Academy of Sciences, China) for providing statistical PS-*r*-PMMA. The authors thank the National Natural Science Foundation of China (Grant Nos. 61974030 and 21925301) and Zhangjiang Laboratory for supporting this work.

Appendix A. Supplementary data

Supplementary data to this article can be found online at https://doi.org/10.1016/j.heliyon.2024.e24016.

References

[1] M.J. Rees, On the future: a keynote address, Engineering 6 (2020) 110–114.
[2] J. Houghton, Global warming, Rep. Prog. Phys. 68 (2005) 1343–1403.
[3] R.A. Kerr, Global warming is changing the world, Science 316 (2007) 188–190.
[4] X. Zhao, X. Ma, B. Chen, Y. Shang, M. Song, Challenges toward carbon neutrality in China: strategies and countermeasures, Resour. Conserv. Recycl. 176 (2022) 105959.
[5] Intel Intel Climate Change Policy Statement, 2020. https://www.intel.com/content/www/us/en/corporate-responsibility/environment-climate-change-policy.html.
[6] N. Kannan, D. Vakeesan, Solar energy for future world: a review, Renew. Sust. Energ. Rev. 62 (2016) 1092–1105.
[7] L.A. Weinstein, J. Loomis, B. Bhatia, D.M. Bierman, E.N. Wang, G. Chen, Concentrating solar power, Chem. Rev. 115 (2015) 12797–12838.
[8] D. Fernández-González, A state-of-the-art review on materials production and processing using solar energy, Miner. Process. Extr. Metall. Rev. (2023) 1–43.
[9] S.K. Sansaniwal, V. Sharma, J. Mathur, Energy and exergy analyses of various typical solar energy applications: a comprehensive review, Renew. Sust. Energ. Rev. 82 (2018) 1576–1601.
[10] X.-H. Hu, R. Zhang, Z. Wu, S. Xiong, Concentrated solar induced graphene, ACS Omega 7 (2022) 27263–27271.
[11] B. Xu, B. Lin, Reducing carbon dioxide emissions in China's manufacturing industry: a dynamic vector autoregression approach, J. Clean. Prod. 131 (2016) 594–606.
[12] A. Hasanbeigi, M. Arens, J.C.R. Cardenas, L. Price, R. Triolo, Comparison of carbon dioxide emissions intensity of steel production in China, Germany, Mexico, and the United States, Resour. Conserv. Recycl. 113 (2016) 127–139.
[13] Ernst Worrell, Lynn Price, Nathan Martin, L.O. Chris Hendriks, Meida. Carbon dioxide emissions from the global cement industry, Annu. Rev. Environ. Resour. 26 (2001) 303–329.
[14] U. Gupta, Y.G. Kim, S. Lee, J. Tse, H.H.S. Lee, G.Y. Wei, D. Brooks, C.J. Wu, Chasing carbon: the elusive environmental footprint of computing, IEEE Micro (2021) 854–867.
[15] J. Porter, TSMC Earmarks Record $44 Billion for Chip Manufacturing Expansion in 2022, 2022. https://www.theverge.com/2022/1/13/22881576/tsmc-capital-investment-2022-chip-manufacturer-demand-increase.
[16] D. Nordell, Planned U.S. Semiconductor Manufacturing Growth and the Middle Market, 2021. https://rsmus.com/what-we-do/industries/technology-companies/planned-us-semiconductor-manufacturing-growth-and-the-middle-mar.html.
[17] G. Leopold, Global Chip Boom Driving Foundry Expansion, 2021. https://www.eetasia.com/global-chip-boom-driving-foundry-expansion/.
[18] E. Mullen, M.A. Morris, Green nanofabrication opportunities in the semiconductor industry: a life cycle perspective, Nanomaterials 11 (2021) 1085.
[19] Y. Chen, S. Xiong, Directed self-assembly of block copolymers for sub-10 nm fabrication, Int. J. Extrem. Manuf. 2 (2020) 032006.
[20] X.-H. Hu, S.-S. Xiong, Advanced lithography: directed self-assembly, Chin. J. Appl. Chem. 38 (2021) 1029–1078.
[21] X.-H. Hu, S. Xiong, Fabrication of nanodevices through block copolymer self-assembly, Front. Nanotechnol. 4 (2022) 762996.
[22] Z. Li, X. Hu, S. Xiong, DSA in combination with DUV lithography for sub-10 nm manufacturing, Laser Optoelectron. Prog. 59 (2022) 0922027.
[23] Z.-L. Li, X.-R. Xu, J.-H. Zhan, X.-H. Hu, Z.-Y. Zhang, S.-S. Xiong, Advanced materials for lithography, Chin. J. Appl. Chem. 39 (2022) 859–870.
[24] C.-C. Liu, E. Franke, Y. Mignot, R. Xie, C.W. Yeung, J. Zhang, C. Chi, C. Zhang, R. Farrell, K. Lai, H. Tsai, N. Felix, D. Corliss, Directed self-assembly of block copolymers for 7 nanometre FinFET technology and beyond, Nat. Electron. 1 (2018) 562–569.
[25] H.S. Wang, K.H. Kim, J. Bang, Thermal approaches to perpendicular block copolymer microdomains in thin films: a review and appraisal, Macromol. Rapid Commun. 40 (2019) 1800728.
[26] M. Ceresoli, F.G. Volpe, G. Seguini, D. Antonioli, V. Gianotti, K. Sparnacci, M. Laus, M. Perego, Scaling of correlation length in lamellae forming PS-*b*-PMMA thin films upon high temperature rapid thermal treatments, J. Mater. Chem. C 3 (2015) 8618–8624.
[27] K. Sparnacci, D. Antonioli, M. Perego, T.J. Giammaria, G. Seguini, F. Ferrarese Lupi, G. Zuccheri, V. Gianotti, M. Laus, High temperature surface neutralization process with random copolymers for block copolymer self-assembly, Polym. Int. 66 (2017) 459–467.
[28] X. Zhang, K.D. Harris, N.L.Y. Wu, J.N. Murphy, J.M. Buriak, Fast assembly of ordered block copolymer nanostructures through microwave annealing, ACS Nano 4 (2010) 7021–7029.
[29] C. Jin, J.N. Murphy, K.D. Harris, J.M. Buriak, Deconvoluting the mechanism of microwave annealing of block copolymer thin films, ACS Nano 8 (2014) 3979–3991.
[30] P.W. Majewski, K.G. Yager, Millisecond ordering of block copolymer films *via* photothermal gradients, ACS Nano 9 (2015) 3896–3906.
[31] P.W. Majewski, A. Rahman, C.T. Black, K.G. Yager, Arbitrary lattice symmetries *via* block copolymer nanomeshes, Nat. Commun. 6 (2015) 7448.
[32] A.A. Leniart, P. Pula, A. Sitkiewicz, P.W. Majewski, Macroscopic alignment of block copolymers on silicon substrates by laser annealing, ACS Nano 14 (2020) 4805–4815.
[33] J. Jiang, A. Jacobs, M.O. Thompson, C.K. Ober, Laser spike annealing of DSA photoresists, J. Photopolym. Sci. Technol. 28 (2015) 631–634.
[34] H.M. Jin, D.Y. Park, S.-J. Jeong, G.Y. Lee, J.Y. Kim, J.H. Mun, S.K. Cha, J. Lim, J.S. Kim, K.H. Kim, K.J. Lee, S.O. Kim, Flash light millisecond self-assembly of high χ block copolymers for wafer-scale sub-10 nm nanopatterning, Adv. Mater. 29 (2017) 1700595.
[35] E.C. Giraud, T. Ghoshal, M.A. Morris, Observation of ordered microphase separation of block copolymer micellar thin films under argon-plasma radiation, Appl. Surf. Sci. 561 (2021) 149800.
[36] A. Hieno, S. Hattori, H. Nakamura, K. Asakawa, Y. Seino, M. Kanno, T. Azuma, Quick Formation of DSA neutralization polymer layer attached by reactive self-assembled monolayer, J. Photopolym. Sci. Technol. 25 (2012) 73–76.
[37] L. Oria, A. Ruiz de Luzuriaga, J.A. Alduncin, F. Perez-Murano, Polystyrene as a brush layer for directed self-assembly of block Co-polymers, Microelectron. Eng. 110 (2013) 234–240.
[38] H. Kato, Y. Seino, H. Yonemitsu, H. Sato, M. Kanno, K. Kobayashi, A. Kawanishi, T. Imamura, M. Omura, N. Nakamura, T. Azuma, Electrical via chain yield for DSA contact hole shrink process, J. Photopolym. Sci. Technol. 26 (2013) 21–26.

[39] X. Chevalier, C. Nicolet, R. Tiron, A. Gharbi, G. Chamiot-Maitral, K. Jullian, P. Pimenta-Barros, M. Argoud, J.-L. Peyre, R. Van Spaandonk, G. Fleury, G. Hadziioannou, C. Navarro, Self-assembly of high-resolutions PS-*b*-PMMA block-copolymers: processes capabilities and integration on 300 mm track, Proc. SPIE 9049 (2014) 90490Y.
[40] S. Ouk Kim, H.H. Solak, M.P. Stoykovich, N.J. Ferrier, J.J. de Pablo, P.F. Nealey, Epitaxial self-assembly of block copolymers on lithographically defined nanopatterned substrates, Nature 424 (2003) 411–414.
[41] S. Ji, W. Liao, P.F. Nealey, Block cooligomers: a generalized approach to controlling the wetting behavior of block copolymer thin films, Macromolecules 43 (2010) 6919–6922.
[42] R.A. Segalman, H. Yokoyama, E.J. Kramer, Graphoepitaxy of spherical domain block copolymer films, Adv. Mater. 13 (2001) 1152–1155.
[43] J. Chai, D. Wang, X. Fan, J.M. Buriak, Assembly of aligned linear metallic patterns on silicon, Nat. Nanotechnol. 2 (2007) 500–506.
[44] M.P. Stoykovich, M. Müller, S.O. Kim, H.H. Solak, E.W. Edwards, J.J. de Pablo, P.F. Nealey, Directed assembly of block copolymer blends into nonregular device-oriented structures, Science 308 (2005) 1442–1446.
[45] R. Ruiz, H. Kang, F.A. Detcheverry, E. Dobisz, D.S. Kercher, T.R. Albrecht, J.J. de Pablo, P.F. Nealey, Density multiplication and improved lithography by directed block copolymer assembly, Science 321 (2008) 936–939.
[46] R.L. Davis, P.M. Chaikin, R.A. Register, Cylinder orientation and shear alignment in thin films of polystyrene–poly(n-hexyl methacrylate) diblock copolymers, Macromolecules 47 (2014) 5277–5285.
[47] Y.C. Kim, T.J. Shin, S.-M. Hur, S.J. Kwon, S.Y. Kim, Shear-solvo defect annihilation of diblock copolymer thin films over a large area, Sci. Adv. 5 (2019) eaaw3974.
[48] S. Jo, S. Jeon, H. Kim, C.Y. Ryu, S. Lee, D.Y. Ryu, Balanced interfacial interactions for fluoroacrylic block copolymer films and fast electric field directed assembly, Chem. Mater. 32 (2020) 9633–9641.
[49] R.M. Jacobberger, V. Thapar, G.-P. Wu, T.-H. Chang, V. Saraswat, A.J. Way, K.R. Jinkins, Z. Ma, P.F. Nealey, S.-M. Hur, S. Xiong, M.S. Arnold, Boundary-directed epitaxy of block copolymers, Nat. Commun. 11 (2020) 4151.
[50] J. Bekaert, J. Doise, V.-K. Murugesan Kuppuswamy, R. Gronheid, B.T. Chan, G. Vandenberghe, Y. Cao, Y. Her, Contact hole multiplication using grapho-epitaxy directed self-assembly: process choices, template optimization, and placement accuracy, Proc. SPIE 9231 (2014) 92310R.